IEEE Robotics and Automation Letters (RAL) paper presented at the
2020 IEEE International Conference on Robotics and Automation (ICRA)
31 May - 31 August, 2020. Paris, France

Development of Visible Manipulator with Multi-Gear Array Mechanism for Laparoscopic Surgery

Haibo Wang, Shuxin Wang and Siyang Zuo, *Member, IEEE*

***Abstract*—In recent years, robotic technology has been introduced to medical fields, and many surgical robots have been proposed for minimally invasive surgery (MIS). However, due to the limitations in dexterity imposed by surgical instruments and occlusion area, surgeons experience great difficulties during operations. In this paper, we propose a visible manipulator for laparoscopic surgery. Unlike other multiple degree-of-freedom (DOF) manipulators that utilize compliant parts or tendons and pulleys, our proposed manipulator adopts a multi-gear array mechanism to perform the yaw and pitch motions. The manipulator is integrated with a visualization unit to provide macroscopic images for observation in a constrained cavity. Moreover, flexible surgical tools with different functions can be inserted through the central channel of the manipulator to perform diagnostic or therapeutic procedures. A master-slave system is developed to control the bending motions. Bending characteristics experiments and load capacity experiments are performed. The experimental results demonstrate that the proposed manipulator can perform bending motions with a yaw angle range of -76.8°~76.2° and a pitch angle range of -75.2°~75.6°. The manipulator can lift a workload of 250 g during yaw motion and a workload of 150 g during pitch motion, demonstrating the potential clinical value of the visible manipulator for robot-assisted surgery.**

***Index Terms*—Medical robots and systems, mechanism design.**

I. Introduction

Currently, minimally invasive surgery (MIS) has attracted great attention due to its distinct advantages in minimizing invasiveness, including less blood loss, shorter hospital stay, and relatively less pain [1]. Laparoscopic surgery, a common type of MIS, has been adapted to various surgical procedures because it can minimize the morbidity and potential mortality associated with laparotomies [2, 3]. In laparoscopic surgery, the surgeon inserts laparoscope, forceps and other surgical instruments into the abdominal cavity through small holes attached with trocars. In some high risk laparoscopic procedures, surgeons need to manipulate these instruments to pass through the cramped or tortuous paths and perform surgery in narrow cavities that the hand and eye are unable to access. However, traditional surgical instruments, such as laparoscope and the corresponding operating tools, lack the flexibility to perform procedures in a narrow and deep area of the abdominal cavity [4]. Surgical instruments with higher flexibility [5] are suitable for approaching these limited cavities. However, flexible instruments have low stiffness, which affects the stability of manipulation [6]. Thus, there is an increasing demand for the development of multiple degree-of-freedom (DOF) surgical instruments with high stability and flexibility.

Recent developments in this research area include a 6-DOF manipulator for minimally invasive fetal surgery [7], a controllable stiffness manipulator for laparoendoscopic single-site surgery (LESS) [8] and 5-DOF robotic instruments for endoscopic surgery [9]. These multi-DOF manipulators [7-9] use rolling-joints and wire-driven mechanisms to transfer force and power from the actuator to the bendable portion. The wire is easily bent and can change the direction of the applied force, enabling the wire-driven mechanism to minimize the manipulator. However, the low stiffness and wearing and tearing of thin wire are practical difficulties to consider [10]. Furthermore, the long-term operation can permanently extend the length of wire, resulting in a large gap between the drive wire and rolling-joint, which greatly degrades the performance of the manipulator. The high tension applied to the wire can help solve the gap problem, but increases the possibility of wire breakage to some extent [11].

To solve the high tension and breakage problem of the wire-driven mechanism, many other multi-DOF manipulators that utilize different driving methods have been developed. For example, some research institutions have developed manipulators based on a linkage-driven mechanism [12-14]. Compared to the wire that can only sustain extension, the linkage can sustain both compression and extension. However, these complex structures require high machining accuracy and assembly accuracy [15]. Another driven mechanism is the screw-driven mechanism. Research in this area includes a multi-DOF forceps manipulator based on double-screw-drive (DSD) mechanism [16]. However, the backlash of the universal joint inevitably resulted in wobbling in the bending part [17]. Gear-based methods have also been applied to surgical manipulators. For example, Mart *et al*. proposed a positioning apparatus controlled by a gear-driven actuator [18]. However, the positioning apparatus can only be bent in one plane. Chen *et al*. proposed a laparoscopic forceps manipulator based on a gear-driven mechanism [19]. Since the gear was driven by a synchronous belt, and slipping and deformation of the belt affect the performance of the manipulator [20]. The DragonFlex laparoscopic instrument incorporated gears into the rolling joint to resist tangent forces and prevent slippage [21]. However, since it was

Manuscript received: September 9, 2019; Revised: November 20, 2019; Accepted: January 25, 2020. This paper was recommended for publication by Editor Paolo Rocco upon evaluation of the Associate Editor and Reviewers′ comments. This work was supported by the Key Technologies Research and Development Program of China under Grant No. 2019YFB1311501 and National Natural Science Foundation of China under Grant No. 61773280. (Corresponding author: Siyang Zuo.)

Haibo Wang, Shuxin Wang and Siyang Zuo are with Key Laboratory of Mechanism Theory and Equipment Design of Ministry of Education, Tianjin University, Tianjin 300072, China (e-mail: haibo_wang@tju.edu.cn; shuxinw@tju.edu.cn; siyang_zuo@tju.edu.cn)

Digital Object Identifier (DOI): see top of this page.

driven by wires, wearing and tearing remains an inevitable issue [10].

In addition, some research institutions have focused on developing manipulators using a direct-drive style by arranging actuators inside the bending parts of the manipulator. For example, Ayvali *et al*. proposed shape memory alloy (SMA) actuators that were annealed in an arc shape to perform a specific controlled bending motion [22]. Ho *et al*. used two antagonistic SMA wires as an actuator for each bending joint [23]. Since the characteristic of SMA actuators can only change between the original shape and the pre-deformed shape, the SMA behavior is nonlinear, hysteretic, and extremely temperature dependent [24]. In addition, the SMA was heated by the Joule effect of current. Therefore, it is not safe to use in the human body [10]. Another direct-drive style is the motor-driven mechanism, which fixes the micromotor directly into the manipulator and individually actuates the bending motion of each joint [25]. The motor-driven mechanism can perform relatively precise bending motion, but the size and output force of the manipulator are limited by the micromotor [26].

In this study, we proposed a visible manipulator that uses a mechanically coupled multi-gear array mechanism to provide the yaw and pitch motions for laparoscopic surgery (Fig. 1). The manipulator can be used as a bendable endoscope. Hence, flexible surgical tools with different functions can be inserted through the working channel and operate under the endoscopic view of the integrated visualization unit. In the following section, we report 1) the mechanical design of the multi-gear array mechanism, 2) the mechanical characteristics analysis of the proposed manipulator, 3) the load capacity performance, 4) the endoscopic function evaluation of the integrated visualization unit. The experimental results demonstrate that proposed visible manipulator is feasible in laparoscopic surgery.

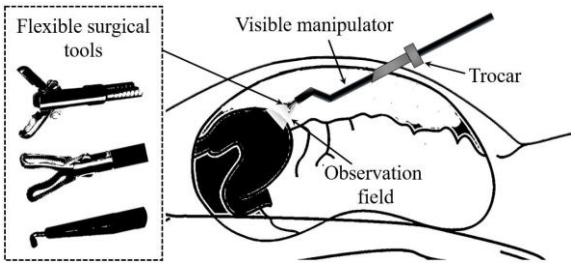

Fig.1 Concept of visible manipulator in laparoscopic surgery.

II. Methods

A. System Configuration

The system configuration of the proposed visible manipulator, as shown in Fig. 2, consists of three parts. The first part is the bendable end-effector. The multi-gear array mechanism can perform the yaw and pitch motions. The insertion part of the manipulator is fixed to the actuation package but can be separated from the actuation package for sterilization. The integrated visualization unit consists of a micro-camera and lighting module, which can provide macroscopic images in the constrained cavity. The second part is the actuation package, which contains two brushless DC-servomotors and Hall sensors. The DC-servomotors are coupled to the bending mechanism for actuating the yaw and

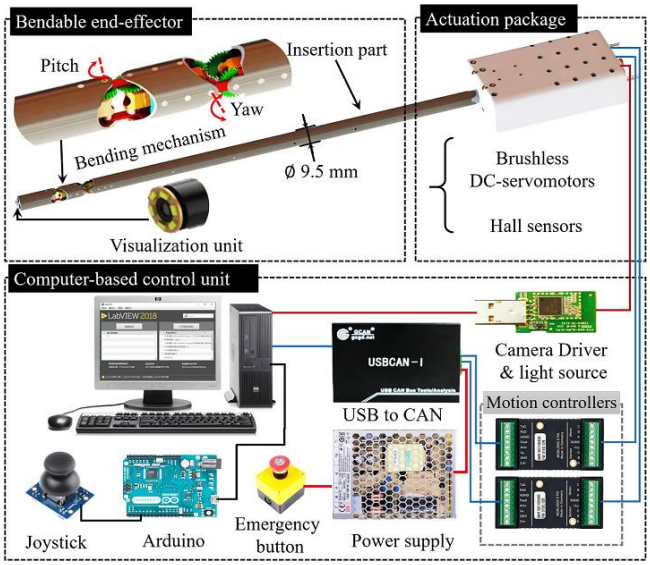

Fig.2 The system configuration of visible manipulator consists of a bendable end-effector with multi-gear array mechanism and visualization unit, an actuation package with brushless DC-servomotors and Hall sensors, and a computer-based control unit.

pitch motions. The Hall sensors can form a servo system with the motion controllers to achieve precise control of the DC-servomotors. The third part is the computer-based control unit. A customized user interface was developed in LabVIEW (National Instruments Corp., USA) to initialize parameters, control the manipulator, and record data. The joystick can communicate with software to manipulate the visible manipulator. In addition, the control unit was designed with an emergency button to stop the operation in case of an accident. In an emergency, we can cut off the power and separate the insertion part from the actuation package, thereby releasing the shape lock of the bending part. As a result, the manipulator can be safely removed from the trocar without harming the patient.

B. Bendable End-effector

The proposed bendable end-effector based on multi-gear array mechanism, as shown in Fig. 3, has the ability to perform the yaw and pitch motions. The end-effector has a maximum outer diameter of 9.5 mm and includes a central channel with a diameter of 3 mm for passing surgical tools and a side channel greater than 5.6 mm × 1.6 mm for arranging signal lines of the visualization unit. The detail compositions of the bending body include spur gears, bevel gears, pins, shaped gears, racks and connection frames.

Yaw motion is performed by the first articulated section. Shaped gear 1 is fixed to base frame 2 and meshes with gear set 1. Spur gear 1 meshes with gear set 1 and the racks at the same time. All spur gears are connected together by the connection frames. Thus, when the racks move synchronously, the end-effector performs the yaw motion through the transmission of the spur gears.

Pitch motion is performed by the second articulated section. The two bevel gears mesh with each other, and spur gear 2 is coupled with bevel gear using a pair of pins. The two spur gears 2 meshes with gear set 2 and spur gear 3, respectively. Gear set 2 meshes with gear set 1. Shaped gear 2 is fixed to base frame 3 and meshes with spur gear 3. Thus, when only

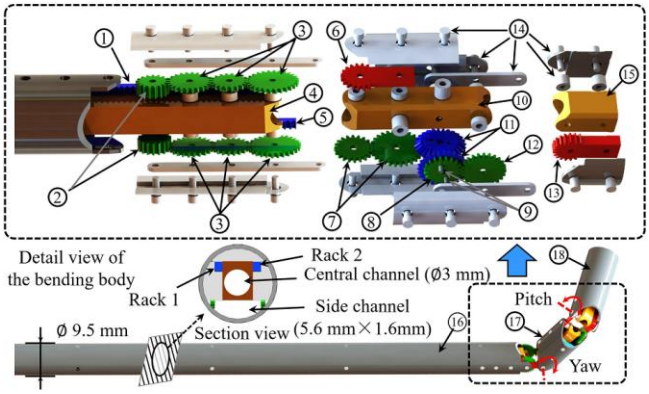

Fig.3 Configuration and detailed view of the bendable end-effector: ① rack 1, ② spur gears 1, ③ gear set 1, ④ base frame 1, ⑤ rack 2, ⑥ shaped gear 1, ⑦ gear set 2, ⑧ spur gears 2, ⑨ pin, ⑩ base frame 2, ⑪ bevel gears, ⑫ spur gear 3, ⑬ shaped gear 2, ⑭ connection frames, ⑮ base frame 3, ⑯ outer frame 1, ⑰ outer frame 2, ⑱ outer frame 3.

rack 2 moves and rack 1 remains stationary, the end-effector performs the pitch motion through the transmission of the spur gears and the steering of the bevel gears.

Finite element analysis (FEA) was carried out using ANSYS Workbench (Ansys Inc., USA) to analyze the stress generated in the manipulator under various force loads. Since the joints are the weak parts, we performed FEA of the joint and internal meshing gears. Fig. 4 shows the stress and deformation of the second articulated section when load forces of 5 N and 7 N are applied to the tip of the manipulator. Considering the yield strength of stainless steel (SUS304), the proposed manipulator can maintain a stable shape under a load force of 5 N, which is sufficient for laparoscopic surgery.

C. Actuation Package

The actuation package, as shown in Fig. 5(a), includes bevel gears, spur gears, pins and DC-servomotors. Bevel gear 1 and bevel 2 meshes with each other. The spur gear is coupled with bevel gear 2 using a pair of pins and meshes

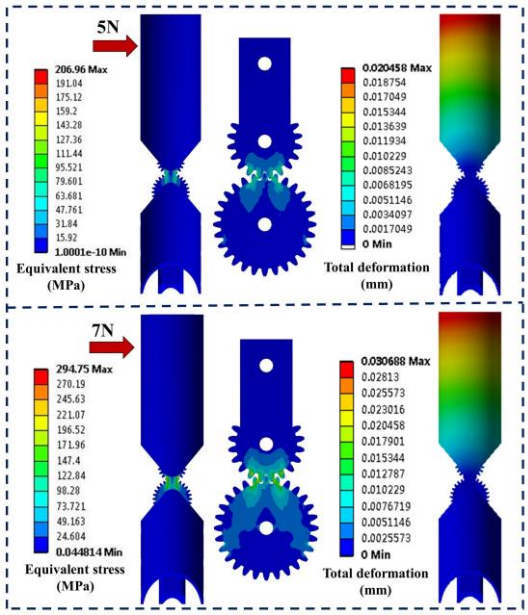

Fig.4 FEA simulation results of the stress and deformation generated in the joint and internal meshing gears under load forces of 5 N and 7 N.

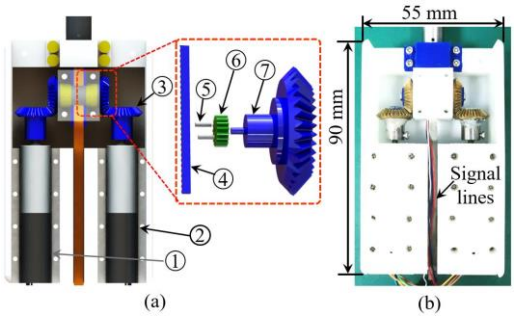

Fig.5 Actuation package of the manipulator, showing (a) the configuration of the actuation package: ① DC-servomotor 1, ② DC-servomotor 2, ③ bevel gear 1, ④rack, ⑤ pin, ⑥ spur gear, ⑦bevel gear 2, (b) the photo of the actuation package.

with the rack. A high-resolution brushless DC-servomotor (1226 E 012 B, Faulhaber SA, Germany) equipped with an 879:1 zero backlash gearhead (Series 12/5, Faulhaber SA, Germany) is connected to bevel gear 1, which can provide a high output torque of 1.73 Nm to actuate the bending motions. The prototype of the actuation package is shown in Fig. 5(b), the signal lines of the visualization unit were led out through the side channel. A 55 mm × 25 mm × 90 mm rectangular cover was used to enclose the actuation package.

D. Kinematic Analysis and Control Algorithms

For the proposed manipulator, the bending angle can be controlled by inputting corresponding commands to the DC-servomotors. The end-effector was designed to perform bending motions with $\theta \in [-80°, 80°]$ and $\beta \in [-80°, 80°]$. The kinematics and design parameters of the bending body are shown in Fig. 6(a, b). The linear displacements of the racks, l_1 and l_2, bend the articulated sections by θ and β. The kinematic relationship can be expressed by the following equations:

$$\theta = \frac{360^{\circ}}{\pi \cdot m \cdot z} \cdot l_1 \tag{1}$$

$$\beta = \frac{360^{\circ}}{\pi \cdot m \cdot z} \cdot l_2 \tag{2}$$

where m and z are the modulus and number of teeth of the shaped gears, as shown in Fig. 3.

As mentioned above, the linear displacements of the racks are driven by the DC-servomotors. The relationship between rack displacement and motor rotation can be expressed as follows:

$$l = \frac{\pi \cdot m \cdot z_1}{\mu \cdot 360^{\circ}} \cdot \alpha \tag{3}$$

where m and z_1 are the modulus and number of teeth of the spur gear as shown in Fig. 5. μ is the reduction ratio of the gearhead, and α is the rotation angle of the DC-servomotor.

The complete expression of the bending angle can be given by (4) and (5), and the kinematic relationship is shown in Fig. 6(c).

$$\theta = \frac{z_1}{z \cdot \mu} \cdot \alpha_1 \tag{4}$$

$$\beta = \frac{z_1}{z \cdot \mu} \cdot \alpha_2 \tag{5}$$

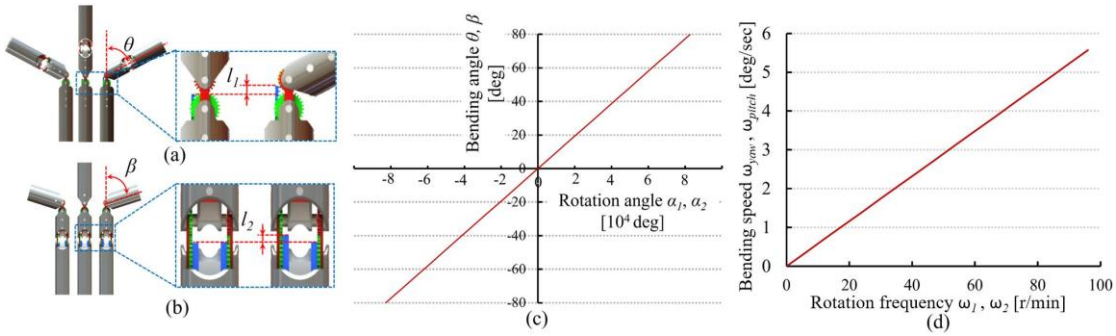

Fig.6 Kinematics analysis of the bendable end-effector, showing (a) the design parameters of the first articulated section, (b) the design parameters of the second articulated section, (c) the kinematic relationship between the bending angle and motor rotation angle, and (d) the kinematic relationship between bending speed and the rotation frequency of the motor.

where α_1 is the angle that the two DC-servomotors rotate synchronously, α_2 is the rotation angle that the DC-servomotor 2 rotates alone.

The expression for the bending speed can be given by (6) and (7), and the kinematic relationship is shown in Fig. 6(d).

$$\omega_{\text{yaw}} = \frac{z_1}{z \cdot \mu} \cdot \omega_1 \tag{6}$$

$$\omega_{\text{pitch}} = \frac{z_1}{z \cdot \mu} \cdot \omega_2 \tag{7}$$

where ω_{yaw} and ω_{pitch} are the bending speeds of the yaw motion and pitch motion, respectively. ω_1 is the rotation frequency that the two DC-servomotors rotate synchronously, ω_2 is the rotation frequency that the DC-servomotor 2 rotates alone.

In this study, every servomotor has an integrated magnetic encoding system (analogue Hall sensor (K1855, Faulhaber SA, Germany)) that allows for closed-loop position control using a dedicated motion controller (MCBL 3002S CF, Faulhaber SA, Germany). In this system, Hall sensor can achieve a position resolution of 3000 increments per revolution of the servomotor. In addition, every servomotor is equipped with an 879:1 zero backlash gearhead, which can further improve the output position resolution. The control strategy of the manipulator is illustrated in Fig. 7. To reduce the influence of the backlash among gears, we use predictive control commands to compensate for the backlash. Using yaw motion as an example, θ_t is the target bending angle input by the joystick, $\Delta\theta_t$ and $\Delta\theta_{t-1}$ are the previous two target bending angle increments. If the bending motions are in the same direction, the motors are controlled directly to rotate the corresponding angle. α_{1t} is the target rotation angle that the motors should rotate. $\Delta\alpha_1$ is the rotation angle increment calculated from the target rotation angle α_{1t} and current rotation angle feedback α_{1f}. V_1 is the corresponding output analog voltage generated by the motion controller for precise rotation angle. If the bending motions are in opposite directions, the motors are controlled to pre-rotate to compensate for the backlash in the gears caused by the change in bending direction. Then, the targeted bending motion is performed. α_{p1} is the pre-rotation angle that the motors should rotate. We found experimentally that the pre-rotation angle was slightly different depending on the bending posture of the end-effector, and the backlash can be effectively compensated when α_{p1} was 15500 degrees. Thus, with the predictive control strategy, yaw motion can be performed with little influence of the backlash among gears. The independent control process of pitch motion is the same as yaw motion.

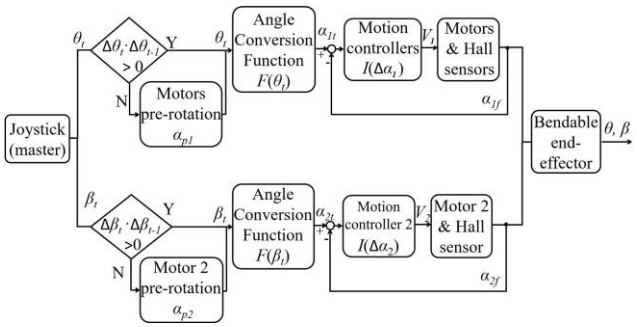

Fig.7 The control strategy for the bending motions.

III. Experimental Results

To verify the manipulator concept and mechanism design, we fabricated a manipulator prototype, as shown in Fig. 8. The constituent materials of the bendable end-effector were stainless steel (SUS304). The manipulator was 9.5 mm in outer diameter, 300 mm in length and 320 g in weight. After manufacturing and assembly, we conducted a series of experiments to evaluate the performance of the manipulator.

A. Mechanical Performance of the End-effector

As the most important feature of the proposed manipulator, bending performance was evaluated first. The experimental setup is shown in Fig. 9(a). A mini gyro sensor (JY61P, WitMotion Shenzhen Co., Ltd., China) with a swing angle accuracy of 0.05° was attached to the tip of the manipulator to measure and record the bending angles. We controlled the bending angle of two articulated sections from 0° to ±80° and returned to 0° in steps of 10° at bending speed of 1°/s. For each bending condition, five repeated trials were performed to compare the actual bending angle and the target angle. The repeatability errors and the relationship between the

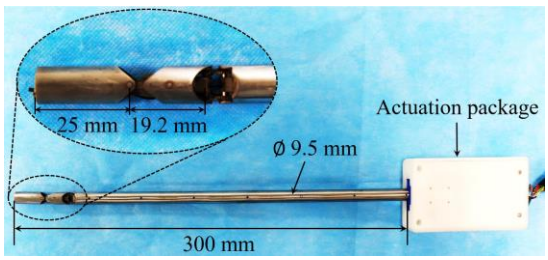

Fig.8 Visible manipulator prototype.

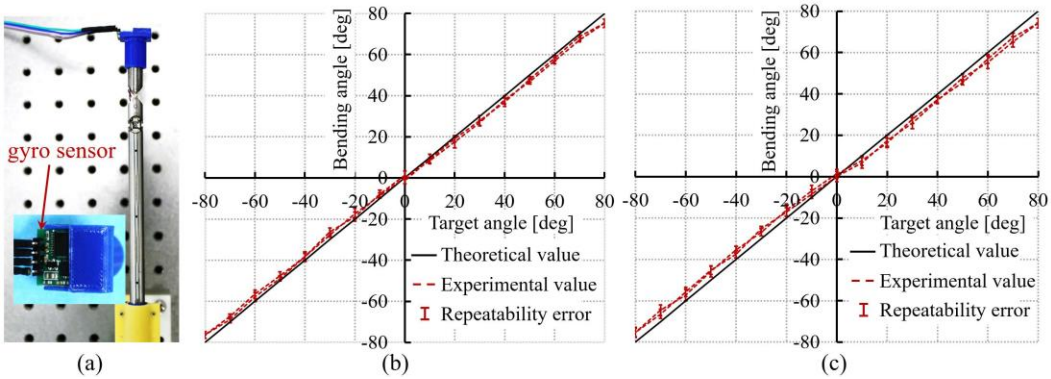

Fig.9 Mechanical performance of the bendable end-effector, showing (a) the experimental setup, (b) the bending performance of the first articulated section, (c) the bending performance of the second articulated section.

experimental bending angles and the theoretical bending angles are shown in Fig. 9(b, c). From the experimental results, the bending motion was roughly consistent with the theoretical expectation. The measured values were -76.8°~76.2° for yaw motion and -75.2°~75.6° for pitch motion. The standard deviations for the yaw motion and pitch motion were 1.6° and 3.5°, respectively.

Then, we evaluated the performance of the manipulator to bend to a specified position. The experimental setup is the same as shown in Fig. 9(a). We controlled the manipulator to bend from the initial position (0°, 0°) to $\theta \in$ {-75°, -45°, -15°, 15°, 45°, 75°} and $\beta \in$ {-75°, -45°, -15°, 15°, 45°, 75°}, for a total of 36 cases. The difference angle γ_{diff} between theoretical expectations and experimental values can be expressed by the following equations:

$$V_{\text{tip, theo}} = ((19.2+25\cos\beta_t)\cdot\cos\theta_t, (19.2+25\cos\beta_t)\cdot\sin\theta_t, 25\sin\beta_t) \quad (8)$$

$$V_{\text{tip, exp}} = ((19.2+25\cos\beta_e)\cdot\cos\theta_e, (19.2+25\cos\beta_e)\cdot\sin\theta_e, 25\sin\beta_e) \quad (9)$$

$$\gamma_{\text{diff}} = \arccos\left(V_{\text{tip, theo}} \cdot V_{\text{tip, exp}}\right) \quad (10)$$

where $V_{\text{tip, theo}}$ and $V_{\text{tip, exp}}$ are the theoretical vector and the experimental vector of the tip direction, respectively. (θ_t, β_t) and (θ_e, β_e) are the theoretical position and experimental position, respectively. The lengths of first articulated section and the second articulated section are 19.2 mm and 25 mm, respectively, as shown in Fig. 8. The experimental results are compared with the theoretical ones in Table I. The average difference is 1.15°.

TABLE I. COMPARISON OF THE TIP DIRECTION BETWEEN THEORETICAL AND EXPERIMENTAL RESULTS

#	$V_{\text{tip, theo}}$ (deg) (θ_t, β_t)	$V_{\text{tip, exp}}$ (deg) (θ_e, β_e)	$\lvert\gamma_{\text{diff}}\rvert$ (deg)	#	$V_{\text{tip, theo}}$ (deg) (θ_t, β_t)	$V_{\text{tip, exp}}$ (deg) (θ_e, β_e)	$\lvert\gamma_{\text{diff}}\rvert$ (deg)
1	75, 75	74.1, 76.3	0.97	*19*	-15, 75	-15.3, 75.4	0.34
2	75, 45	75.3, 46.4	0.82	*20*	-15, 45	-14.4, 44.2	0.69
3	75, 15	74.8, 14.2	0.42	*21*	-15, 15	-17.2, 15.6	2.16
4	75, -15	74.5, -16.1	0.76	*22*	-15, -15	-15.2, -16.3	0.71
5	75, -45	74.4, -46.8	1.10	*23*	-15, -45	-15.7, -43.3	1.14
6	75, -75	75.6, -73.6	1.07	*24*	-15, -75	-17.1, -75.4	0.38
7	45, 75	44.2, 74.3	0.72	*25*	-45, 75	-44.2, 73.4	1.10
8	45, 45	46.4, 44.2	1.40	*26*	-45, 45	-43.3, 47.4	2.03
9	45, 15	43.5, 13.8	1.57	*27*	-45, 15	-46.1, 13.6	1.34
10	45, -15	46.2, -14.2	1.33	*28*	-45, -15	-45.8, -17.2	1.43
11	45, -45	47.2, -43.3	2.26	*29*	-45, -45	-43.7, -43.8	1.39
12	45, -75	43.4, -73.8	1.50	*30*	-45, -75	-44.7, -73.6	0.84
13	15, 75	16.3, 74.6	0.96	*31*	-75, 75	-73.8, 74.2	0.99
14	15, 45	14.2, 46.2	1.01	*32*	-75, 45	-75.2, 47.5	1.40
15	15, 15	16.6, 13.5	1.85	*33*	-75, 15	-74.7, 13.9	0.66
16	15, -15	15.8, -13.3	1.22	*34*	-75, -15	-73.8, -17.6	1.78
17	15, -45	16.3, -46.1	1.33	*35*	-75, -45	-74.8, -42.3	1.18
18	15, -75	15.9, -75.4	0.69	*36*	-75, -75	-75.3, -76.1	0.82

B. Load Capacity of the Manipulator

Load capacity is another important feature of the proposed manipulator. We conducted a series of experiments to examine the amount of weight the manipulator can lift. In the load capacity test, the manipulator was fixed horizontally on the optical platform and controlled to lift the workload from the lower limit position to the upper limit position. The results show that the first articulated section can lift a workload of at least 250 g and the second articulated section can lift a workload of at least 150 g with stable bending motions within the workspace (Fig. 10).

C. Load Capacity of the Manipulator

Based on the system configuration, the visible manipulator can observe the target tissue and surgical tool in the confined cavity. Thus, we performed simplified experiments with a laparoscopic surgery simulator (lyd918, Ningbo Lancet Medical Technology Co., Ltd., China) to evaluate the endoscopic function of the visualization unit (OV9734, Shenzhen Yichuang Electronics Co., Ltd. China). The experimental setup is shown in Fig. 11(a). A shade cloth was used to cover the simulator to create a more realistic surgical environment. The visible manipulator was mounted on a tripod and inserted into the simulator through a minimally invasive keyhole, and then controlled to observe and capture endoscopic images of the target colored beads. In this

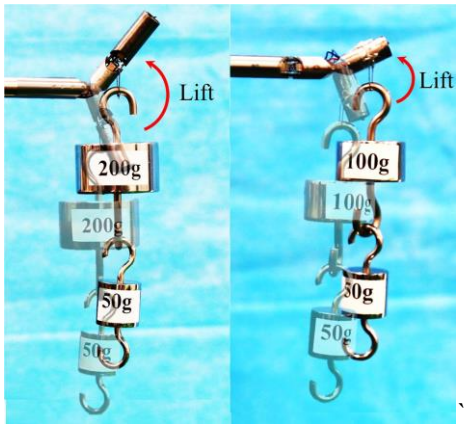

Fig.10 Load capacity of the manipulator.

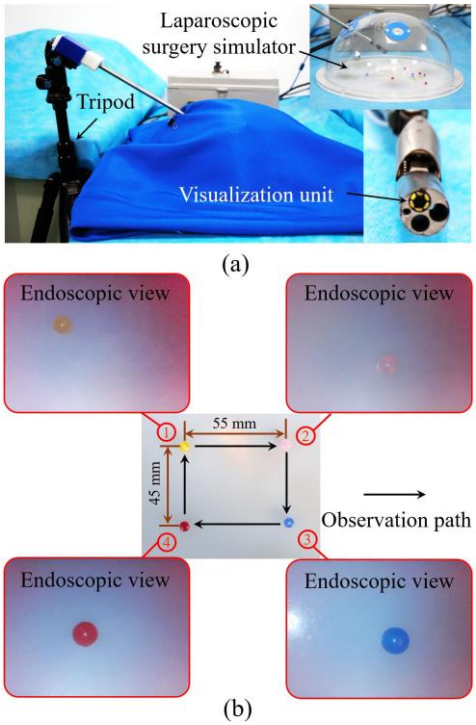

Fig.11 The endoscopic function of the visualization unit, showing (a) the experimental setup, (b) the captured endoscopic images of the target colored beads.

experiment, the operator controlled the manipulator to observe along a rectangular path at a bending speed of 1°/s and repeated the experiment five times. The experiment took approximately 43 seconds on average to complete the observation of the four colored beads. The captured endoscopic images of the four colored beads are shown in Fig. 11(b), indicating that the manipulator can identify the situation and reach the target location in a constrained cavity without the requirement of additional endoscopes.

Then, we combined forceps with the manipulator to evaluate the endoscopic function, as shown in Fig. 12 (a). In this experiment, we controlled the manipulator to grab the target (10g Standard Weight) in the laparoscopic surgery simulator. The experimental results are shown in Fig. 12 (b),

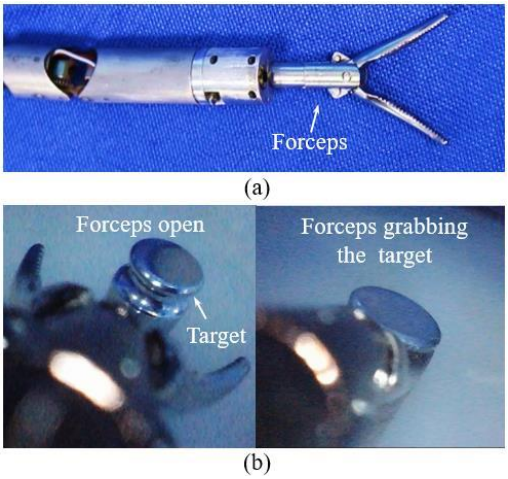

Fig.12 Functional evaluation of visualization unit, showing (a) the forces combined with the visible manipulator, (b) the target and forceps remain within the FOV of the captured endoscopic images.

where the forceps and target remain within the field of view (FOV) of the captured endoscopic images. This indicates that the proposed visible manipulator has the capacity to perform corresponding procedures under real-time image observation of the integrated visualization unit.

IV. Discussion

A novel visible manipulator based on multi-gear array mechanism is proposed in this paper. The main contributions and features of this paper include: 1) the mechanically coupled multi-gear array mechanism and motor control strategy based on predictive control algorithms that enable the manipulator to perform relatively accurate yaw and pitch motions, 2) the rigid rack and gear structure enables reliable power transmission and can lock the shape of the manipulator through gear meshing, 3) the integrated visualization unit allows *in situ* image observation without requiring additional endoscopes, 4) flexible surgical tools that can be assembled and switched with the visible manipulator to enrich diagnostic or therapeutic functions. However, the surgical tools must be inserted through the working channel before the manipulator performs bending motions. In addition, the proposed visible manipulator can be mounted on a commercially available robot arm (e.g., LBR Med, KUKA AG, Germany) to adjust and maintain a suitable interventional position for surgical procedures.

In Table II, we summarized the multi-DOF manipulators aimed at performing complex diagnostic or therapeutic procedures in narrow cavities. Compared with the wire-driven mechanism [5, 7-9], the proposed multi-gear array mechanism has advantages in terms of stiffness, wearing and tearing; Compared with the linkage-driven mechanism [13], our proposed manipulator can bend in two orthogonal planes. In addition, high-precision machining technology (wire-cut EDM) can ensure accuracy of the mechanical components of the manipulator; Compared with the SMA actuator [27], the proposed manipulator is not affected by the ambient temperature; Compared with the motor-driven mechanism [23, 24], the size of our manipulator is not limited to the motor used; Compared with previous gear-based forceps manipulator [28], our proposed manipulator has a smaller outer diameter and larger bending range. In addition, our proposed manipulator has a 3 mm

TABLE Ⅱ. Comparison with other multi-DOF manipulator

Description	Wang *et al.*[5]	Shi *et al.*[27]	Zhang *et al.* [13]	Iwamori *et al.*[28]	This work
Driving mechanism	Wire-driven	SMA actuation	linkage-driven	gear-driven	gear-driven
Outer diameter	Tip:9 mm; Root:30 mm	8 mm	10 mm	12 mm	9.5 mm
Degrees of freedom	Infinite number	2	2	4	2
Bending range	-	order of 120°	order of 170°	order of 120°	order of 150°
Manipulate force	-	-	3 N	-	1.5 N
Endoscopic function	Yes	No	Yes	No	Yes
Working channel	Yes	No	No	No	Yes
Stiffness	Low	Medium	High	High	High

working channel for passing through flexible surgical tools. A visualization unit is integrated with the manipulator to observe the target tissue and surgical tool in the constrained cavity and avoid area occlusion.

The mechanical performance of the end-effector indicates that the manipulator has the capability to perform two-axis bending motions. Theoretically, the manipulator can perform bending motions in the range of ±80°. However, due to assembly errors and contact restrictions among the mechanical components, the actual bending range of the first articulated section was between -76.8° and 76.2°, and the actual bending range of the second articulated section was between -75.2° and 75.6°. A wider bending range can be achieved by optimizing the size of the mechanical components.

The predictive control algorithm used to compensate for the backlash in the gears is an effective method to reduce hysteresis. However, from the bending curves, the experimental value are not centered on the theoretical line (Fig. 9(b, c)). This is mainly caused by the insufficient pre-rotation angle of the servomotor to compensate for the clearance in the gears and can be improved by increasing the pre-rotation angle appropriately. In addition, there are some deviations between the experimental and theoretical values. This is mainly caused by the clearances in the gears. In addition, gyroscope drift can affect measurement accuracy. In this study, the mini gyro sensor obtained data from the internally integrated three-axis accelerometer and three-axis gyroscope chip. Then, a Kalman filter was used to reduce measurement noise, thereby ensuring relatively accurate measurements. The experimental results show that the manipulator can bend to the specified position with an average difference of 1.15°. The bending performance can be further optimized by optimizing gear parameters, reducing redundant gears, using anti backlash spur gears and improving the manufacturing accuracy and assembly accuracy.

Load capacity test results show that the multi-gear array mechanism has the inherent advantage of high rigidity. In this prototype, the first articulated section can lift a workload of 250 g and the second articulated section can lift a workload of 150 g, indicating that the proposed manipulator can provide a manipulation force of approximately 1.5 N. A previous study showed that a manipulation force of 1.5 N is sufficient and safe for manipulating tissues such as large bowel, small bowel and peritoneum [29]. When a larger load is lifted, the slender rack inside the manipulator as shown in Fig. 5 will undergo a slight elastic deformation under the contact force between the gear and rack, resulting in the discontinuous lifting process. The load capacity can be increased by increasing the thickness of the gears and racks, designing components that limit rack deformation, which requires comprehensive considerations of the connection frames and central channel. In addition, the load capacity can also be increased by using more rigid materials such as titanium or titanium alloy to manufacture the racks and gears.

Currently, multi-port laparoscopic surgery (MLS) usually requires 4 holes in the abdominal cavity, followed by inserting the corresponding instruments such as endoscope and surgical tools through the trocars to perform the operation. The proposed visible manipulator can be considered a surgical tool. Thus, it is compatible with the current endoscope without changing the current surgical procedure. In addition, due to the mutual occlusion between surgical tools, some areas are difficult to observe, resulting in a certain risk when performing surgery. Our proposed manipulator is designed with a working channel, the flexible surgical tool can pass though the working channel and perform corresponding procedures under the FOV from both the visible manipulator and endoscope, thereby avoiding the problem of area occlusion. Hence, when the target is in the deep area of abdominal cavity, such as kidney, pancreas and the reverse side of the stomach, it is difficult be observed using the rigid endoscope. Our proposed visible manipulator has the capability to approach, observe and manipulate these tissues in deep area of human body with small invasion (without cutting or lifting tissues or organ in front of the targeted tissues in deep area of abdominal cavity).

In this study, the visualization unit used in the manipulator can capture endoscopic images at 30 fps for live display to the user. The user did not sense an image delay at all. Thus, it is satisfied with real-time use requirements. The delay time of the manipulator is affected by many factors such as the sample update rate, communication rate, algorithm time-consumption and motor response speed. We used a high-speed industrial camera (OSG030-815UC, Shenzhen Yingshi Technology Co., Ltd., China) to capture the video from the motion commands input to the beginning of the bending motion at 200 fps for measuring time-delay. We found experimentally that the system's delay time is less than 150 milliseconds, which can meet real-time operation requirements.

In the endoscopic function evaluation, it took an average of 43 seconds to complete the observation task (Fig. 11(b)). The time it takes to complete the task depends on the bending speed and the skill of the operator, which can be reduced by increasing the bending speed. However, due to the limited performance of the micro-camera, such as the focus distance and FOV, the captured image as shown in Fig. 12(b) is not as clear as commercially available endoscope and cannot generate a large overview. Nevertheless, the images captured by the visualization unit are acceptable for observing the targets in the closed cavity. Furthermore, a medical micro-CCD camera with higher resolution (e.g., IntroSpicio™ 110, Medigus, Inc. Israel) can replace the visualization unit to provide a wider FOV and larger overview, which requires further research.

The actuation package and computer-based control unit enable master-slave control of the manipulator, allowing easy operation for first-time users. However, due to analog output errors of the joystick, some end-effector bending motions cannot be performed accurately according to the user's operation. A more accurate master-slave control system can be developed by replacing the joystick with the commercial sensible phantom Omni haptic device (3D Systems, SC, USA).

The sterilization of the manipulator is an essential issue to address. Due to internal heat-sensitive components, the sterilization of the proposed visible manipulator can be achieved using a low temperature steam formaldehyde

method, ultrasonic cleaning, or soaking method with 2.4% glutaraldehyde [30].

In addition, there are still areas for improvement for future applications. First, the mechanical design and components should be optimized to minimize the diameter. Second, we will explore an additional DOF for roll motion by placing a micromotor at the end-effector tip or utilizing a flexible shaft delivered through the side channel of the manipulator. The rolling motion will significantly increase the potential clinical value of the manipulator. Moreover, Fiber Bragg grating (FBG) sensors [31-33] can be used in the proposed manipulator to estimate the 3D shape of the end-effector and measure the contact force. Finally, the diagnosis and surgical tools that can be assembled and switched with the visible manipulator will be explored in the future.

V. Conclusion

In this study, we developed a visible manipulator with a multi-gear array mechanism for laparoscopic surgery. A master-slave control system was built to control the manipulator. Fundamental experiments were performed to examine the bending performance, load capacity and endoscopic function of the proposed manipulator. The experimental results showed that the manipulator can perform two-axis bending motions with a yaw angle range of -76.8°~76.2° and a pitch angle range of -75.2°~75.6°. The proposed manipulator can lift a workload of 250 g during yaw motion and a workload of 150 g during pitch motion. Moreover, with the integrated visualization unit, the manipulator can provide endoscopic images of the targeted location in a constrained cavity. These experimental results demonstrate the potential clinical value of the proposed visible manipulator in robot-assisted surgery.

References

[1] Y. Vellani, S. Bhatti, G. Shamsi, Y. Parpio, and T. S. Ali, "Evaluation of laparoscopic appendectomy vs. open appendectomy: a retrospective study at Aga Khan University Hospital, Karachi, Pakistan," *J. Pak. Med. Assoc.*, vol. 59, no. 9, pp. 605-608, 2009.

[2] H. J. Bonjer *et al*., "A randomized trial of laparoscopic versus open surgery for rectal cancer," *N. Engl. J. Med*., vol. 372, no. 14, pp. 1324-1332, 2015.

[3] M. Alfa-Wali, and S. Osaghae, "Practice, training and safety of laparoscopic surgery in low and middle-income countries," *World. J. Gastrointest. Surg.*, vol. 9, no. 1, pp.13-18, 2017.

[4] M. Cianchetti *et al*. "Soft robotics technologies to address shortcomings in today's minimally invasive surgery: the STIFF-FLOP approach," Soft robotics, vol. 1, no. 2, pp. 122-131, 2014.

[5] H. Wang, R.Zhang, W. Chen, X. Wang, and R. Pfeifer, "A cable-driven soft robot surgical system for cardiothoracic endoscopic surgery: preclinical tests in animals," *Surg. Endosc*., vol. 31, no. 8, pp. 3152-3158.2017.

[6] L. lanc *et al*., "Flexible medical devices: review of controllable stiffness solutions," *Actuators.,* vol. 6, no. 3, pp. 23, 2017.

[7] B. Zhang *et al*., "Development of 6-DOF wire-driven robotic manipulator for minimally invasive fetal surgery," in *Proc. IEEE Int. Conf. Robot. Autom.*, May. 2011, pp. 2892-2897

[8] J. Wang *et al*., "Development of a novel robotic platform with controllable stiffness manipulation arms for laparoendoscopic single‐site surgery (LESS)," *Int. J. Med. Robot. Comp*., vol. 14, no. 1, e1838, 2018.

[9] P. Berthet-Rayneet *et al*., "The i^2 snake robotic platform for endoscopic surgery," *Ann. Biomed. Eng*., vol. 46, no. 10, pp. 1663-1675, 2018.

[10] H. M. Le *et al*., "A survey on actuators-driven surgical robots," *Sens. Actuators. A. Phys*., 247, pp. 323-354, 2016.

[11] D. C. Friedman *et al*., "Instrument failures for the da Vinci Surgical System: a Food and Drug Administration MAUDE database study," *Surg. Endosc.,* vol. 27, no. 5, pp. 1503-1508, 2013.

[12] H. Yamashita, D. Kim, N. Hata, and T. Dohi, "Multi-slider linkage mechanism for endoscopic forceps manipulator," In *Proceedings 2003 IEEE/RSJ International Conference on Intelligent Robots and Systems*, Oct. 2003, Vol. 3, pp. 2577-2582.

[13] B. Zhang, Z. Liao, P. Yang, and H. Liao, "Robotic Visible Forceps Manipulator With a Novel Linkage Bending Mechanism," *J. Mech. Robot*., vol. 11, no. 1, 011012, 2019.

[14] S. Zuo, M. Hughes, and G. Yang, "Novel Balloon Surface Scanning Device for Intraoperative Breast Endomicroscopy," *Ann. Biomed. Eng*., vol. 44, no. 7, pp. 2313–2326, 2016.

[15] D. Haraguchi, T. Kanno, K. Tadano, and K. Kawashima, "A pneumatically driven surgical manipulator with a flexible distal joint capable of force sensing," *IEEE ASME Trans. Mechatron*., vol. 20, no. 6, pp. 2950-2961, 2015.

[16] C. Ishii, and T. Futatsugi, "Design and control of a robotic forceps manipulator with screw-drive bending mechanism and extension of its motion space," *Procedia CIRP*, 5, pp. 104-109, 2013.

[17] C. Ishii, K. Kobayashi, Y. Kamei, and Y. Nishitani, "Robotic forceps manipulator with a novel bending mechanism," *IEEE ASME Trans. Mechatron*., vol. 15, no. 5, pp. 671-684, 2009.

[18] M. A. Minor, and R. Mukherjee, U.S. Patent No. 6,309,403. Washington, DC: U.S. Patent and Trademark Office, 2001.

[19] S. P. Chen *et al*., "Flexible Laparoscopic Forceps Manipulator using Synchronous Belt Mechanism," *Applied Mechanics and Materials*., vol. 607, pp. 303-306, Trans Tech Publications, 2014.

[20] V. Eliseev, and Y. Vetyukov, "Effects of deformation in the dynamics of belt drive," *Acta. Mech*., vol. 223, no. 8, pp. 1657-1667, 2012.

[21] F. Jelínek, and P. Breedveld, "Design for additive manufacture of fine medical instrumentation—DragonFlex case study," *J. Mech. Design.*, vol. 137, no. 11, 111416, 2015.

[22] E. Ayvali, and J. P. Desai, "Towards a discretely actuated steerable cannula," in *Proc. IEEE Int. Conf. Robot. Autom*., May. 2012, pp. 1614-1619.

[23] M. Ho, and J. P. Desai, "Characterization of SMA actuator for applications in robotic neurosurgery," *In 2009 Annual International Conference of the IEEE Engineering in Medicine and Biology Society*., Sep. 2009, pp. 6856-6859.

[24] S. Barbarino *et al*., "A review on shape memory alloys with applications to morphing aircraft," *Smart. Mater. Struct*., vol. 23, no. 6, 063001, 2014.

[25] J. Shang *et al*., "An articulated universal joint based flexible access robot for minimally invasive surgery," in *Proc. IEEE Int. Conf. Robot. Autom*. 2011, pp. 1147-1152.

[26] M. Piccigallo *et al*., "Design of a novel bimanual robotic system for single-port laparoscopy," *IEEE ASME Trans. Mechatron*., vol. 15, no. 6, pp. 871-878, 2010.

[27] Z. Shi *et al*., "A compact and stiffer shape memory alloy actuator for surgical instruments," in *Proc. IEEE Int. Conf. Mech. Autom*., Aug. 2016, pp. 477-484.

[28] Y. Iwamori *et al*., "Multi-DOF Forceps Manipulator for an Approach to the dorsal aspect of an Organ," In World Congress on Medical Physics and Biomedical Engineering., Springer, Berlin, Heidelberg. pp. 4164-4168, 2007.

[29] S. P. Rodrigues *et al*., "Suturing intraabdominal organs: when do we cause tissue damage?" *Surg. Endosc.*, vol. 26, no. 4, pp.1005-1009, 2012.

[30] W. A. Rutala, and D. J. Weber, "Guideline for disinfection and sterilization in healthcare facilities," 2008.

[31] Z. Wang, S. Wang, and S. Zuo, "A Hand‐held Device with 3‐DOF Haptic Feedback Mechanism for Microsurgery." *Int. J. Med. Robot. Comp*., e2025, 2019.

[32] N. Rahman *et al*., "Modular FBG Bending Sensor for Continuum Neurosurgical Robot". *IEEE Robot. Autom. Lett.*, vol. 4, no. 2, pp. 1424-1430, 2019.

[33] Wei, S. Wang, J. Li, and S. Zuo, "Novel integrated helical design of single optic fiber for shape sensing of flexible robot," *IEEE Sens. J.*, vol. 17, no. 20, pp. 6627-6636, 2017.